Journal of Biomedical Optics

BiomedicalOptics.SPIEDigitalLibrary.org

Near-infrared indocyanine dye permits real-time characterization of both venous and lymphatic circulation

Toshikazu Kurahashi
Katsuyuki Iwatsuki
Tetsuro Onishi
Tetsuya Arai
Katsunori Teranishi
Hitoshi Hirata

SPIE.

Toshikazu Kurahashi, Katsuyuki Iwatsuki, Tetsuro Onishi, Tetsuya Arai, Katsunori Teranishi, Hitoshi Hirata, "Near-infrared indocyanine dye permits real-time characterization of both venous and lymphatic circulation," *J. Biomed. Opt.* **21**(8), 086009 (2016), doi: 10.1117/1.JBO.21.8.086009.

Near-infrared indocyanine dye permits real-time characterization of both venous and lymphatic circulation

Toshikazu Kurahashi,[a,b] Katsuyuki Iwatsuki,[a,*] Tetsuro Onishi,[a] Tetsuya Arai,[c] Katsunori Teranishi,[d] and Hitoshi Hirata[a]
[a]Nagoya University, Department of Hand Surgery, 65 Tsurumai-cho, Showa-ku, Nagoya 466-8550, Japan
[b]Anjo Kosei Hospital, Hand and Microsurgery Center, 28 Higashihirokute, Anjo-cho, Anjo 446-8602, Japan
[c]Gifu Prefectural Tajimi Hospital, Department of Orthopedic Surgery, 5-161 Maehata-cho, Tajimi 507-8522, Japan
[d]Mie University, Department of Life Sciences, Regulatory Biochemistry, 1577 Kurimamachiya-cho, Tsu 514-8507, Japan

Abstract. We investigated the optical properties of a near-infrared (NIR) fluorochrome, di-β-cyclodextrin-binding indocyanine derivative (TK-1), and its pharmacokinetic differences with indocyanine green (ICG). TK-1 was designed to have hydrophilic cyclodextrin molecules and, thus, for higher water solubility and smaller particle sizes than the plasma protein-bound ICG. We compared optical properties such as the absorption and fluorescence spectra, quantum yield, and photostability between both dyes *in vitro*. In addition, we subcutaneously injected a 1 mM solution of TK-1 or ICG into the hind footpad of rats and observed real-time NIR fluorescence intensities in their femoral veins and accompanying lymphatics at the exposed groin site to analyze the dye pharmacokinetics. These optical experiments demonstrated that TK-1 has high water solubility, a low self-aggregation tendency, and high optical and chemical stabilities. Our *in vivo* imaging showed that TK-1 was transported via peripheral venous flow and lymphatic flow, whereas ICG was drained only through lymphatics. The results of this study showed that lymphatic and venous transport can be differentially regulated and is most likely influenced primarily by particle size, and that TK-1 can enable real-time NIR fluorescence imaging of whole fluids and solute movement via both microvessels and lymphatics, which conventional ICG cannot achieve. [DOI: 10.1117/1.JBO.21.8.086009]

Keywords: fluorescence imaging; near-infrared; indocyanine green; nanoparticles; lymphatics; TK-1.

Paper 160093RR received Feb. 16, 2016; accepted for publication Jul. 25, 2016; published online Aug. 17, 2016.

1 Introduction

Understanding the fluid mechanics of the interstitium is indispensable for a variety of clinical situations and research areas, including immunology, pharmacokinetics, and oncology. However, even such fundamental issues as the regulatory mechanism and route of solute movement between microvessels, the interstitium, and the lymphatics have yet to be elucidated.[1]

In the past decade, optical imaging technology, such as molecular imaging of living tissues with fluorescence emission, has been rapidly developed for the noninvasive evaluation of disease progression or drug effects. When visualizing fluorescent contrast agents existing in deep tissues, absorption and scattering of the excitation and fluorescence emission light by many biocomponents can be serious technical issues. In addition, autofluorescence, i.e., the natural emission of light by certain biological molecules, interferes with and obscures the detection of extrinsic fluorescent contrast agents, causing structures other than those of interest to become visible and manifest as a high background signal, which reduces the image contrast and clarity.[2] Near-infrared (NIR) light in the wavelength range of 700 to 900 nm can be used to overcome these issues. The absorption coefficient of physiological tissues is relatively low in the NIR region than in the visible light region.[3–5] Furthermore, using the excitation light in the NIR region can prevent tissue autofluorescence.[2,6] As a result, NIR light can penetrate into deep tissues and visualize the fluorescent contrast agents existing in those tissues, with a high contrast between the optical signals and the background fluorescence. Organic dyes and inorganic quantum dots (QDs) are two representative NIR fluorescent contrast agents that are currently available in the biomedical fields for both animal testing and clinical applications.[7] Indocyanine green (ICG), a member of the NIR heptamethine indocyanine fluorochromes, is the US Food and Drug Administration (FDA)-approved and can be used safely in humans. Thus, it has been widely employed for *in vivo* optical imaging, such as fluorescent angiography, sentinel lymph nodes (SLN) mapping, and lymphangiography.[8–13] The molecular weight of ICG is 775 Da. ICG is water soluble because of its sulfonyl groups, but can form dimers and oligomers in aqueous solution. These aggregates cause self-quenching of ICG, which reduces its fluorescence in water. When administered to living tissues, ICG rapidly binds to plasma proteins such as albumin, globulins, or lipoproteins[14–16] and then becomes fluorescent under NIR light. The *in vivo* dynamics of ICG, therefore, are defined by those plasma proteins. When considering lymphatic and venous uptake from the interstitial fluid, the behavior of nanoparticles is greatly dependent on the particle size.[17–21] The particle size of plasma protein-bound ICG becomes ~7 to 22 nm in diameter;[16] thus,

*Address all correspondence to: Katsuyuki Iwatsuki, E-mail: kiwatsuki@med.nagoya-u.ac.jp

1083-3668/2016/$25.00 © 2016 SPIE

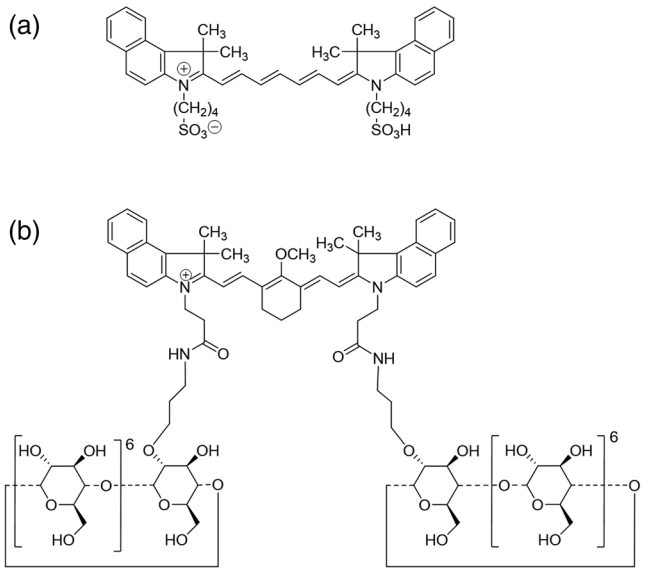

Fig. 1 Structural formulas of ICG and TK-1. (a) ICG is an amphiphilic molecule; two polycyclic groups interconnected by a carbon chain impart lipophilicity to the ICG molecule, and the sulfate groups are responsible for the hydrophilic nature. (b) TK-1 has two hydrophilic cyclic sugar chain β-cyclodextrins.

fluorescent imaging using ICG can only partially reveal the overall movement of materials because it cannot demonstrate the movement of small materials (i.e., less than a few nanometers). Inorganic QDs, which are composed of a semiconductor core commonly made from CdSe or CdTe coated with an inorganic shell, are nanometer-sized fluorescent probes with unique optical and electronic properties. QDs have high quantum yields, high chemical and optical stabilities,[22–25] and tunable characteristics depending on the size and doping characteristics of the nanocrystals.[25] Thus, QDs represent a promising and powerful approach for *in vivo* tumor imaging or targeted drug delivery.[22,26–28] However, the safety of QDs remains a serious concern because toxic elements are present in their cores.[29,30]

To address these problems, we developed an NIR fluorochrome that is a di-β-cyclodextrin-binding indocyanine derivative (named here as TK-1), which has two hydrophilic cyclic sugar chain cyclodextrins (Fig. 1). Here, we determined the optical properties of TK-1 *in vitro* in comparison with ICG. In addition, we report that the lymphatic and venous transport of fluorescent contrast agents, TK-1 and ICG, was differentially regulated depending on their particle sizes, based on real-time fluorescence imaging results in rats.

2 Materials and Methods

2.1 *Materials*

All solvents and chemicals were of reagent grade and were used without further purification. *N*-[(3-(anilinomethylene)-2-chloro-1-cyclohexen-1-yl)methylene]-aniline monohydrochloride (**2**), methanol, sodium acetate, ethyl acetate, acetone, potassium *tert*-butoxide (*t*-BuOK), aqueous HCl, 1-hydroxy-1*H*-benzotriazole monohydrate (HOBt), 1-ethyl-3-(3-dimethylaminopropyl)carbodiimide hydrochloride, *N*,*N*-dimethylformamide (DMF), pyridine, trifluoroacetic acid (TFA), phosphate-buffered saline (PBS; pH 7.4), and dimethylsulfoxide (DMSO) were purchased from Wako Pure Chemical Industries, Ltd. (Osaka, Japan). DMSO-d_6 and D_2O were purchased from Sigma-Aldrich (St. Louis, Missouri). ICG was purchased from MP Biomedicals, LLC (Solon, OH). The compound 1,1,2-trimethyl[1*H*]-benz[*e*]indole-3-propanoic acid (**1**) was prepared as described previously,[31] as was 2A-*O*-(3-aminopropyl)-β-cyclodextrin (**5**).[32] Reversed-phase column chromatography was performed using a Fuji Silysia Chromatorex DM1020T ODS gel. Synthesis reactions were monitored by high-performance liquid chromatography-photodiode array-mass spectrometry (HPLC-PDA-MS).

2.2 *Instruments*

^{1}H and ^{13}C NMR spectra were recorded on a JEOL JNM-A500 spectrometer operating at 500 and 125 MHz, respectively. Chemical shift values and coupling constants are reported as δ (ppm) and J (Hz), respectively. HPLC-PDA-MS analysis was performed using a JASCO Gulliver HPLC system equipped an MD-910 detector and a Waters ZQ 4000 mass spectrometer. The HPLC instrument was equipped with a Cosmosil 5C18-MS column (4.6 mm × 150 mm), and an elution rate of 0.8 mL/min was used. HPLC solvents consisted of water containing 0.1% TFA (solvent A) and methanol containing 0.1% TFA (solvent B). The elution protocol for analytical HPLC began with 100% A, followed by a linear gradient to 100% B over 30 min and held at 100% B for 10 min. Mass analyses were performed in electrospray ionization-positive and -negative modes. High-resolution mass analysis was performed using a Thermo Fisher Scientific, Inc. Orbitrap Velos ETD mass spectrometer. UV-visible-NIR absorption spectra were obtained on a JASCO V-530DS spectrometer using a quartz cell (Hellma, 10-mm light path length) or a micro cell (JASCO, 1.0-mm light path length). Fluorescence spectroscopic studies were performed either in a fluorescence cell (Hellma, 10 × 10 mm) or in a triangular fluorescence cell (JASCO FSA-410) with a JASCO FP-6600 spectrofluorometer.

2.3 *Synthesis of TK-1*

A mixture of 1,1,2-trimethyl[1*H*]-benz[*e*]indole-3-propanoic acid (**1**) (2.25 g, 6.23 mmol), *N*-[(3-(anilinomethylene)-2-chloro-1-cyclohexen-1-yl)methylene]-aniline monohydrochloride (**2**) (1.05 g, 2.92 mmol), and sodium acetate (2.5 g, 30 mmol) in methanol (50 mL) was stirred at 20°C for 60 min. After 1.0 mM aqueous HCl (20 mL) and water (400 mL) were added to the resulting mixture, the precipitate was collected by filtration, followed by sequential washing with 1.0 mM aqueous HCl (100 mL), water (700 mL), ethyl acetate (200 mL), a mixture of ethyl acetate (25 mL) and acetone (25 mL), and ethyl acetate (400 mL), after which it was dried under vacuum to afford 3-(2-carboxyethyl)-2-[2-[3-[2-[3-(2-carboxyethyl)-1,3-dihydro-1,1-dimethyl-2H-benz[e]indol-2-ylidene]ethylidene]-2-chloro-1-cyclohexen-1-yl]ethenyl]-1,1-dimethyl-1H-benz[e]indolium, inner salt (**3**) (1.70 g, 83%). The purity of **3** was checked by HPLC-PDA-MS analysis, and **3** was used without further purification. To a mixture of **3** (0.17 g, 0.243 mmol) and anhydrous methanol (5.0 mL), we added *t*-BuOK (0.3 g, 2.68 mmol) at 20°C, and the resulting reaction mixture was protected from light and stirred at 20°C for 12 h. The reaction was checked for completion by HPLC-PDA-MS. Subsequently, 1 mM aqueous HCl (3.0 mL) was added, and the resulting mixture was added to water (50 mL). After the mixture was evaporated

under reduced pressure to remove the methanol, the precipitate was collected by filtration, followed by washing with water, and dried under vacuum to afford 3-(2-carboxyethyl)-2-[2-[3-[2-[3-(2-carboxyethyl)-1,3-dihydro-1,1-dimethyl-2H-benz[e]indol-2-ylidene]ethylidene]-2-methoxy-1-cyclohexen-1-yl]ethenyl]-1,1-dimethyl-1H-benz[e]indolium (**4**) (0.17 g, 100%), as a green solid. The purity of **4** was checked by HPLC-PDA-MS and ^{1}H NMR analyses, and **4** was used without further purification because of its excellent purity. ^{1}H NMR (500 MHz, DMSO-d_6, 27°C, DMSO: 2.49 ppm): δ 1.8 (2H, m), 1.86 (12H, s), 2.57 (4H, m), 2.62 (4H, t, $J = 6.7$ Hz), 4.43 (4H, t, $J = 6.7$ Hz), 6.29 (2H, d, $J = 14.0$ Hz), 7.44 (2H, t, $J = 8.5$ Hz), 7.60 (2H, t, $J = 8.5$ Hz), 7.69 (2H, d, $J = 8.5$ Hz), 7.98 (2H, d, $J = 8.5$ Hz), 8.01 (2H, d, $J = 8.5$ Hz), 8.03 (2H, d, $J = 14.0$ Hz), 8.20 (2H, d, $J = 8.5$ Hz). HR-MS (ESI, positive mode): m/z calculated for $[C_{45}H_{46}N_2O_5 + H]^+$ 695.3479; found: 695.3455 $[M + H]^+$.

A mixture of **4** (60 mg, 0.086 mmol), 2A-*O*-(3-aminopropyl)-β-cyclodextrin (**5**) (0.26 g, 0.218 mmol), HOBt (34 mg, 0.22 mmol), and 1-ethyl-3-(3-dimethylaminopropyl)carbodiimide hydrochloride (74 mg, 0.39 mmol) in DMF (0.6 mL) and pyridine (1.2 mL) were stirred at 0°C for 6 h in the dark. The reaction was checked for completion by HPLC-PDA-MS. Acetone (10 mL) was added to the resulting mixture, and the precipitate was collected by filtration, washed with acetone, and dried under vacuum. The solid obtained was dissolved in 0.1% aqueous TFA and purified by C-18 open column chromatography, using 1 mM aqueous HCl and 1 mM HCl/methanol as the elution solvents. The product-containing fractions were evaporated under reduced pressure to remove almost all solvent, without complete evaporation of the solvent (to avoid decomposition of the product), after which acetone was added to the resulting residue to powder the product. The precipitate was collected by filtration, followed by washing with acetone, and dried under vacuum to afford TK-1 as a green powder. The resulting powder was dissolved followed filtration with a 0.2-μm membrane filter, and the filtrate was freeze-dried in the dark to afford TK-1 as a green amorphous powder (0.18 g, 69%). The counter anion in TK-1 was unknown. ^{1}H NMR (500 MHz, D_2O, 40°C, acetone: 2.26 ppm): δ 1.54 (2H, m), 1.68 (2H, m), 1.98 (2H, m), 2.19 (6H, s), 2.20 (2H, m), 2.30 (6H, s), 2.6 to 2.85 (10H, m), 2.95 (2H, m), 3.00 (4H, m), 3.08 (2H, t, $J = 12$ Hz), 3.17 (2H, dd, $J = 3.7$, 9.8 Hz), 3.26 (2H, t, $J = 9.8$ Hz), 3.35 to 4.30 (m), 4.35 (2H, t, $J = 9.2$ Hz), 4.50 (2H, t, $J = 9.2$ H), 4.52 (2H, m), 4.63 (2H, m), 4.87 (2H, d, $J = 3.7$ Hz), 4.95 (d, $J = 3.1$ Hz), 4.97 (2H, d, $J = 3.7$ Hz), 5.08 (2H, d, $J = 3.7$ Hz), 5.15 (2H, d, $J = 4.3$ Hz), 5.25 (2H, d, $J = 3.7$ Hz), 5.29 (2H, d, $J = 3.7$ Hz), 6.30 (2H, d, $J = 14.6$ Hz), 7.58 (4H, m), 7.73 (2H, d, $J = 8.5$ Hz), 7.95 (2H, m), 8.25 (2H, m), 8.32 (2H, d, $J = 14.6$ Hz), 8.35 (2H, d, $J = 8.5$ Hz). ^{13}C NMR (125 MHz, D_2O, 40°C, acetone: 31.04 ppm): δ 21.81 (CH_2), 24.69 (CH_2), 27.69 (CH_2), 28.91(CH_3), 29.28 (CH_3), 35.61(CH_2), 41.16(CH_2), 42.15(CH_2), 51.75 (C), 60.33 (CH_2), 60.70 (CH_2), 60.79 (CH_2), 60.94 (CH_2), 61.11 (CH_3), 61.12 (CH_2), 65.99 (C), 71.40 (CH), 71.93 (C, CH), 72.15 (CH), 72.20 (CH_2), 72.42 (CH), 72.55 (CH), 72.71 (CH), 72.92 (C, CH), 73.31 (CH), 73.39 (CH), 73.40 (CH), 73.68 (CH), 73.84 (CH), 74.51 (CH), 74.96 (CH), 80.06 (CH), 80.80 (CH), 80.98 (CH), 81.97 (CH), 82.48 (CH), 82.79 (CH), 98.47 (CH), 100.34 (CH), 100.90 (CH), 101.56 (CH), 102.65 (CH), 103.04 (CH), 103.12 (CH), 111.28 (CH), 122.62 (CH), 123.82 (C), 125.63 (CH), 128.14 (CH), 128.40 (C), 130.24 (CH), 131.20 (CH), 132.13 (C), 134.72 (C), 140.21 (C), 141.05 (C), 171.33 (C), 173.39 (C), 174.75 (C). Some ^{13}C peaks overlapped. UV-visible-NIR (EtOH, 25°C): $\lambda_{max} = 800$ nm (ε 200,000); UV-visible-NIR (PBS, pH 7.4, 25°C): $\lambda_{max} = 800$ nm (ε 200,000); UV-visible-NIR (DMSO, 25°C): $\lambda_{max} = 809$ nm (ε 180,000); Φ_F (EtOH, 25°C): 0.03; Φ_F (PBS, pH 7.4, 25°C): 0.048; Φ_F (DMSO, 25°C): 0.12; fluorescence (EtOH, 25°C): $\lambda_{max} = 811$ nm; fluorescence (PBS, pH 7.4, 25°C): $\lambda_{max} = 812$ nm; fluorescence (DMSO, 25°C): $\lambda_{max} = 825$ nm; MS (ESI, positive mode): m/z calculated for $[C_{135}H_{197}N_4O_{73}]^+$ 3042, found: 3042 $[M]^+$.

2.4 *Characterization of TK-1*

2.4.1 *Optical properties of the TK-1 probe*

The absorption spectra of TK-1 at several concentrations were recorded in PBS at pH 7.4 at 25°C. The fluorescence spectrum of TK-1 was recorded at a probe concentration of 0.1 μM in PBS at pH 7.4 at 25°C, using a fluorescence cell (10 × 10 mm). The fluorescence quantum yield was determined by comparison with ICG in DMSO (fluorescence quantum yield $\Phi_F = 0.13$ at 25°C),[33] using the following equation:[34]

$$\Phi_{F(TK\text{-}1)} = (A_{ICG}/A_{TK\text{-}1})(F_{TK\text{-}1}/F_{ICG})(n_{TK\text{-}1}/n_{ICG})^2\Phi_{F(ICG)}$$

In this equation, Φ_F is the fluorescence quantum yield, A is the absorbance, F is the area under the fluorescence curve, and n is the refractive index of the solvents.

2.4.2 *Fluorescence studies of TK-1 using human whole blood*

Venous blood was obtained from healthy volunteers using sodium heparin-containing syringes. To determine the relationship between probe concentration and fluorescence, whole blood (0.98 mL) and probe solutions (20 μL) were mixed in PBS at several different probe concentrations in triangular fluorescence cells, and fluorescence spectra were recorded at 25°C, with excitation at 760 nm.

2.4.3 *Photostability studies of TK-1*

Photostability studies were performed by obtaining fluorescence measurements at a TK-1 probe concentration of 0.1 μM in PBS at 25°C. The probe solution was added into the triangular fluorescence cell and continuously exposed to light at 760 nm for 200 min in a spectrofluorometer. Changes in the initial and subsequent fluorescence intensities at 810 nm were recorded (excitation wavelength: 760 nm).

2.5 *Animal Studies*

2.5.1 *NIR imaging*

Real-time animal imaging was performed using a fluorescence stereomicroscope (SZX-RFL2, Olympus, Tokyo, Japan) equipped with a single-band filter set optimized for ICG (ICG-B-000; excitation wavelength 769 ± 20.5 nm, emission wavelength 832 ± 18.5 nm; Semrock Inc., Rochester, New York). All bright-field and fluorescence images were taken by an electron-multiplying, cooled charge-coupled device (CCD) camera (QuantEM 512SC, Photometrics, Tucson, Arizona), which was

mounted on the top of the stereomicroscope. The fluorescence intensity of each image was analyzed by Image J software (National Institutes of Health, Bethesda, Maryland).

2.5.2 *Experimental animal model and surgical procedure*

The animal study protocol was approved by the local animal ethics committee, in accordance with the Regulations for Animal Experiments at Nagoya University and the Japanese Government Animal Protection and Management Law (Act No. 105 of October 1, 1973). Twenty 10-week-old, male Sprague–Dawley rats (Charles River Japan Inc., Kanagawa, Japan) were used in this study, with a mean weight of 350 g. All animals were housed under specific pathogen-free conditions up to the time of the experiments.

All surgical procedures were performed under isoflurane anesthesia using a vaporizer for small animals (SF-B01; DS Pharma Biomedical. Co., Ltd., Osaka, Japan). After removing the body hair covering the lower extremity and groin of each rat, a longitudinal incision was made from the medial thigh to the groin, and the femoral vein and accompanying lymphatics were exposed by retracting the external oblique muscle (Fig. 2). Rats were then placed on a fluorescence stereomicroscope in the supine position. An aqueous solution of TK-1 was prepared by dissolving the green amorphous powder of TK-1 in distilled water. One hundred microliters of a 1 mM solution of TK-1 was injected subcutaneously into the hind footpad at a constant rate (20 μL/ sec) using a 27-gauge needle and a syringe pump (YSP-101, YMC Co., Ltd., Kyoto, Japan). Fluorescence images at the exposed groin site were observed in real time using a fluorescence stereomicroscope and were taken every 5 sec for up to 2 h with a CCD camera. For comparison purposes, we performed the same examination using 100 μL of a 1 mM ICG solution ($n = 5$ per group). The pharmacokinetics of TK-1 and ICG were analyzed by measuring fluorescence intensity in the femoral vein or accompanying lymphatics, using Image J software. A small rectangle for the region of interest (ROI) was selected in the area of the femoral vein or one of accompanying lymphatics that exhibited peak fluorescence, and the average fluorescence intensity of each ROI was plotted as a function of time.

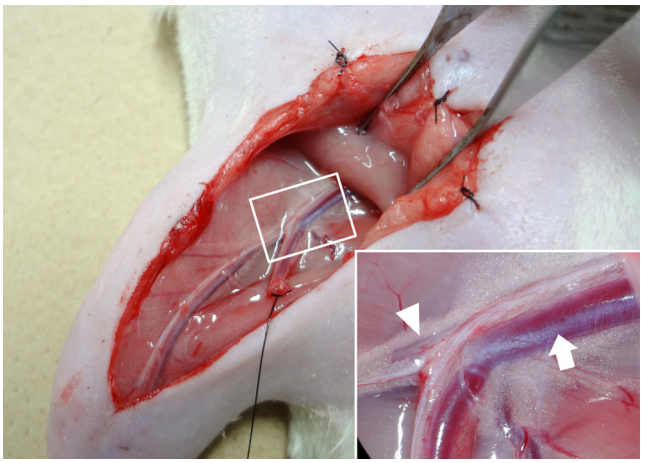

Fig. 2 Surgical field at the groin site of rats. The femoral vein (arrow) and an accompanying lymphatic (arrow-head) were exposed by retracting the external oblique muscle.

In addition, to confirm the presence of fluorescent agents (TK-1 or ICG) within the venous flow, venous blood was collected from the femoral vein at 10 min after injection. After acquiring a drop of venous blood, its fluorescence intensity was calculated using Image J software ($n = 5$ per group). Data were analyzed by performing an unpaired Student t test using SPSS version 19 software (SPSS, Chicago, Illinois); a p-value of <0.05 was considered statistically significant.

3 Results

3.1 *Synthesis of TK-1*

Synthesis of TK-1 was performed as outlined in Fig. 3. Synthesis of intermediate **3**, which contains two carboxylic acid groups that bind with two cyclodextrin molecules, was performed as described previously.[35,36] However, the product yield was not suitable for effective TK-1 preparation. Thus, we developed a convenient and practical high-yield method (83% yield) for preparing compound **3** from **1**.[31] Compound **3** was treated with potassium methoxide prepared from methanol and *t*-BuOK in anhydrous methanol to afford **4** in a quantitative yield. Condensation of **4** with 2A-*O*-(3-Aminopropyl)-β-cyclodextrin [32](**5**) was successfully achieved in DMF/pyridine. The final product (TK-1) was purified using a C-18 open column chromatography, using 1 mM aqueous HCl and 1 mM HCl/methanol, and obtained as a green amorphous powder with a 69% yield. The three-dimensional particle size of TK-1 was calculated by computer-aided analysis. The structure of TK-1 was first drawn in two dimensions with ChemDraw software (PerkinElmer Inc., Waltham, Massachusetts) and then transformed to a three-dimensional structure using ChemBio3D Ultra 13.0 (PerkinElmer Inc., Waltham, Massachusetts). Based on results using these software packages, the largest diameter of TK-1 was calculated to be <3 nm. The effective molecular weight of TK-1 was 3441 Da. TK-1 has two hydrophilic cyclodextrin moieties, which enable water solubility.

3.2 *Optical Properties of TK-1*

The absorption and fluorescence spectra of TK-1 in PBS at pH 7.4 are shown in Fig. 4. The absorbance of TK-1 was found to center at 800 nm ($\varepsilon = 200{,}000\ \mathrm{M}^{-1}\,\mathrm{cm}^{-1}$). As shown in Fig. 4, the shapes of the TK-1 absorption spectra were nearly identical at several concentrations (0.01 to 0.0001 mM), indicating that no or low self-aggregation occurred between the TK-1 molecules. In contrast, the ICG absorbance at 700 nm increased with the ICG concentration, which corresponded to H-aggregation.[6–8] The low self-aggregation property of TK-1 in PBS can be explained by the presence of the two hydrophilic cyclodextrin moieties. The TK-1 fluorescence in PBS at 25°C centered at 812 nm and the TK-1 fluorescence quantum yield (Φ_F) at 25°C was 0.048, which was calculated based on that of ICG in DMSO.[33] This TK-1 quantum yield was slightly higher than that of ICG in PBS at 25°C ($\Phi_F = 0.041$).

The three-dimensional fluorescence spectra of (a) TK-1 and (b) ICG in human venous whole blood at 25°C are shown in Fig. 5 (concentration of TK-1 and ICG: 20 μM). TK-1 showed robust fluorescence excitation over excitation wavelengths ranging from 760 to 780 nm, as did ICG. Figure 6 shows fluorescence-quenching curves for TK-1 and ICG in human venous whole blood at 25°C. In the concentration range of 1 to 200 μM, the TK-1 fluorescence intensity increased in a dose-dependent

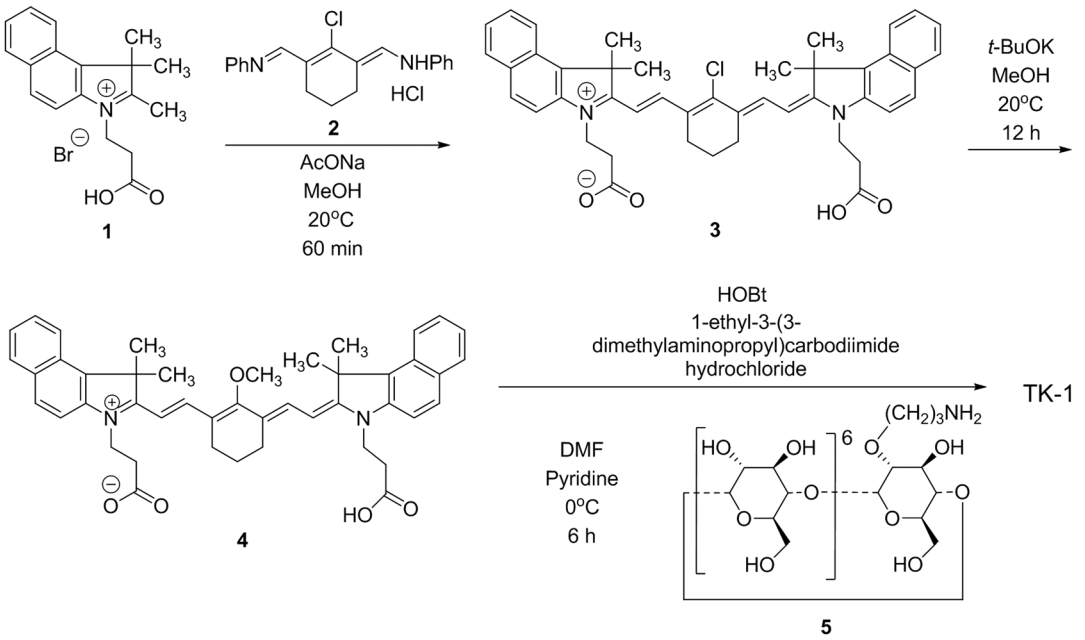

Fig. 3 Synthesis of the di-β-cyclodextrin-bound indocyanine derivative, TK-1, in three steps. Intermediate **4** contains two carboxylic acid groups that bind with two β-cyclodextrin molecules (**5**).

manner, up to the maximum of 200 μM. At higher concentrations, the TK-1 fluorescence was slightly quenched, although the ICG fluorescence was quenched at concentrations exceeding ~40 μM. In addition, the maximum fluorescence peak gradually shifted from 813 to 825 nm with increasing TK-1 concentrations, compared to the marked increase in the wavelength for the maximum fluorescence peak of ICG (Fig. 6). These results indicated that TK-1 showed a lower tendency for aggregation in whole blood than did ICG. A high degree of ICG aggregation decreases its fluorescence intensity, resulting in inaccuracies in fluorescence imaging, while the use of TK-1 can prevent this because it does not aggregate appreciably.

A photostability study of TK-1 and ICG was performed by taking fluorescence measurements (excitation = 760 nm, emission = 810 nm) at a probe concentration of 0.1 μM in PBS at pH 7.4 at 25°C (Fig. 7). When the TK-1 solution was continuously exposed to light at 760 nm, the fluorescence

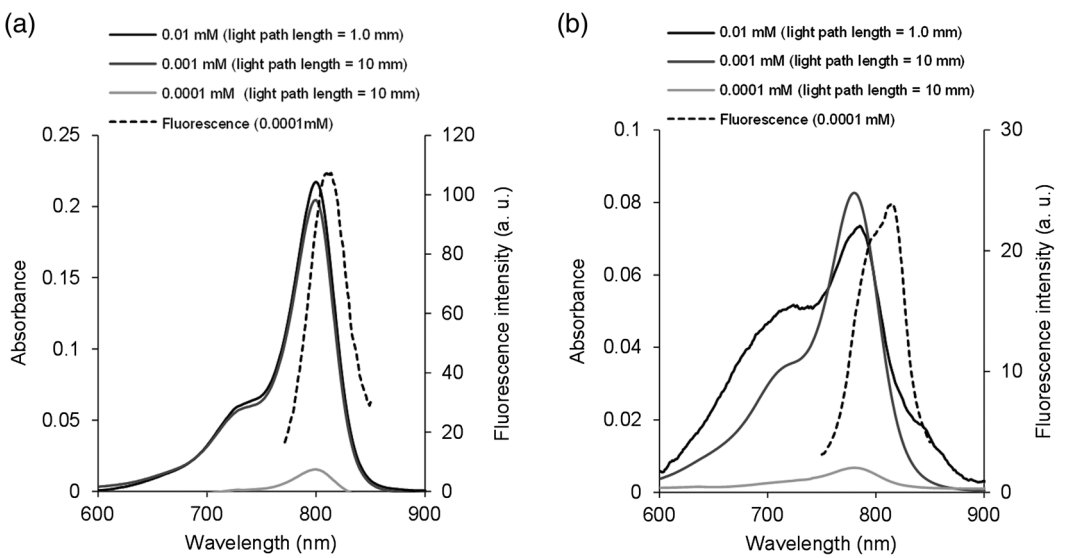

Fig. 4 Absorbance (solid line) and fluorescence (dotted line) spectra of (a) TK-1 and (b) ICG in PBS at pH 7.4 and 25°C. The TK-1 absorbance centered at 800 nm. The shapes of the TK-1 absorption spectra were nearly identical at several concentrations (0.01 to 0.0001 mM), indicating that no or low self-aggregation occurred between the TK-1 molecules. In contrast with TK-1, the shapes of the ICG absorption spectra were not identical at concentrations ranging from 0.01 to 0.0001 mM, indicating that ICG self-aggregates.

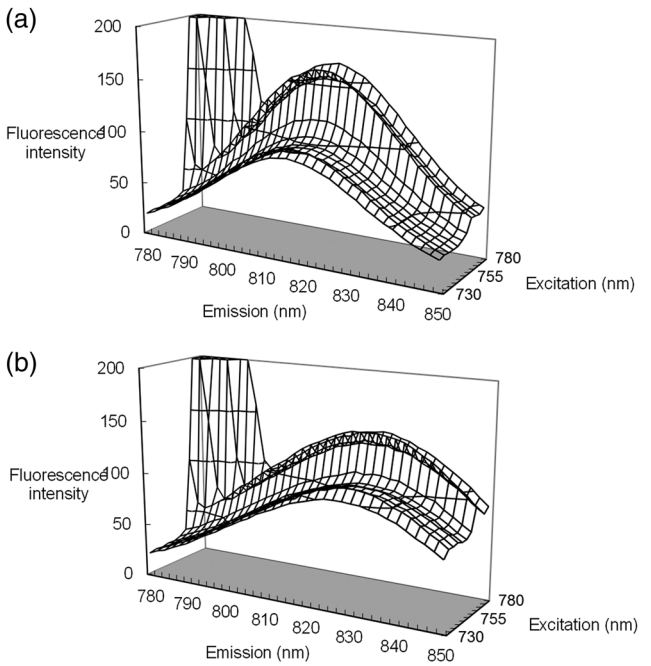

Fig. 5 Three-dimensional fluorescence spectra of (a) TK-1 and (b) ICG in human venous whole blood at 25°C (concentration of TK-1 and ICG: 20 μM). Both TK-1 and ICG showed robust fluorescence excitation at excitation wavelengths 760 to 780 nm.

intensity showed a more gradual decrease over time than did ICG. When not exposed to light, the fluorescence of TK-1 and ICG remained nearly constant.

3.3 *NIR Imaging in Rats*

3.3.1 *Real-time fluorescence imaging*

We obtained continuous fluorescence images at the exposed groin site of rats and analyzed the fluorescence intensity of a femoral vein and accompanying lymphatics, in which TK-1 or ICG was transported. During real-time fluorescence imaging of the TK-1 injected group, the femoral vein was visualized first and successively accompanying lymphatics were then detected, as shown in Fig. 8(a). In the ICG-injected group, most ICG was transported via the lymphatics, as shown in Fig. 8(b). ICG in the femoral vein was not detected. Subsequently, we plotted the time-dependent changes of the average fluorescence intensities of the ROIs defined on the femoral vein and an accompanying lymphatic, which exhibited the peak fluorescence. We found that the transport of TK-1 via lymphatics showed a steep peak at 10 to 15 min after injection, which then decreased immediately to almost the same level as that of the femoral vein [Fig. 9(a)]. In contrast, ICG was transported only through the lymphatics at a nearly constant rate [Fig. 9(b)]. In addition, we performed statistical analysis of the time-dependent data. First, we calculated the average time required for TK-1 and ICG to travel from the footpad to the groin lymphatics. The average time required before detecting the maximum peak of the lymphatic fluorescence was 10.7 ± 3.3 min in the TK-1 group and 24.8 ± 11.6 min in the ICG group ($p < 0.05$). Second, we also calculated the average residence time of TK-1 and ICG in the lymphatics and femoral vein. The average residence time until the lymphatic fluorescence decreased to 20% of the maximum intensity was 67.6 ± 25.7 min in the TK-1 group and 120.0 ± 0.0 min in the ICG group (i.e., ICG remained in the lymphatics for >2 h) ($p < 0.01$). On average, TK-1 remained in the femoral vein for >2 h, whereas ICG was not detected from the beginning.

3.3.2 *Fluorescence intensity of venous blood*

We calculated the intensity of single drops of venous blood from rats in the TK-1-injected and ICG-injected groups, using Image J software. The mean fluorescence intensities of venous blood collected at 10 min were 13824.7 ± 2146.2 and 133.6 ± 11.3 arbitrary units ($p < 0.001$; Fig. 10). These results indicated

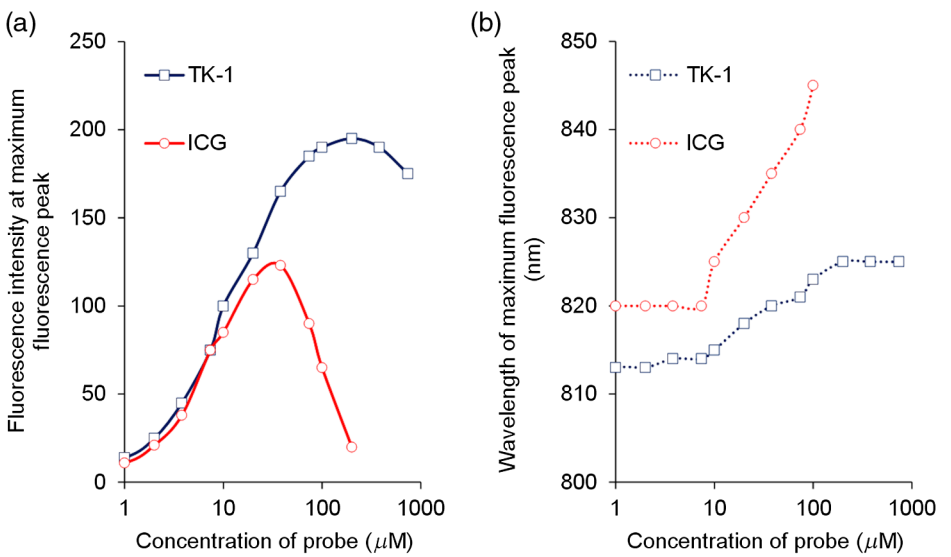

Fig. 6 Relationships between (a) the fluorescence intensity at the maximum fluorescence peak (excitation wavelength: 760 nm), (b) the wavelength of maximum fluorescence peak (excitation wavelength: 760 nm), and the TK-1 and ICG concentrations in human venous whole blood at 25°C. TK-1 showed a tendency for decreased aggregation and low self-quenching in whole blood, compared to that observed with ICG.

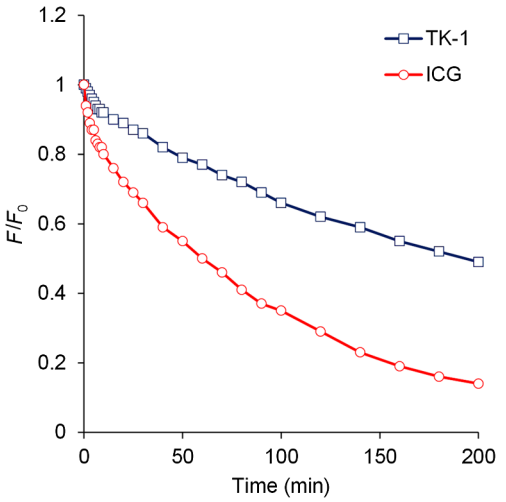

Fig. 7 Photostability of TK-1 and ICG in PBS exposed to 760 nm light at 25°C. F/F_0 is the fluorescence-intensity ratio at 810 nm (excitation wavelength = 760 nm) at the indicated time points (F) to the initial fluorescence intensity (F_0). When the TK-1 solution was continuously exposed to light at 760 nm, the fluorescence intensity decreased more gradually over time than did ICG.

that TK-1 actually infiltrated into the venous flow, whereas ICG did not.

4 Discussion

NIR-excitable fluorescent contrast agents facilitate a broad range of applications for noninvasive *in vivo* imaging, due to their low tissue autofluorescence and deep tissue penetration in this spectral range.[2–6] Regarding NIR fluorochromes that are effective *in vivo* optical imaging, several general properties are desirable, including a high quantum yield, high optical and chemical stabilities, high water solubility, low nonspecific binding, and low toxicity. ICG is an FDA-approved NIR fluorescence-contrast agent that has been widely used for many therapeutic and diagnostic applications, such as cardiac output measurement, liver functional studies, and fluorescence angiography, because it has low toxicity and the capacity to absorb and emit in the NIR spectral region.[8,9,37–40] Recently, ICG fluorescence imaging was also developed for SLN mapping and lymphangiography.[10–13,41–47] However, conventional ICG has several physicochemical disadvantages. ICG is water-soluble because sulfonyl groups are bonded thereto, whereas it has lipophilicity because of the two hydrophobic polycyclic groups.[48,49] Due to its amphiphilic character, ICG has a propensity for adsorbing to lipids. The adhesion or leakage of ICG to

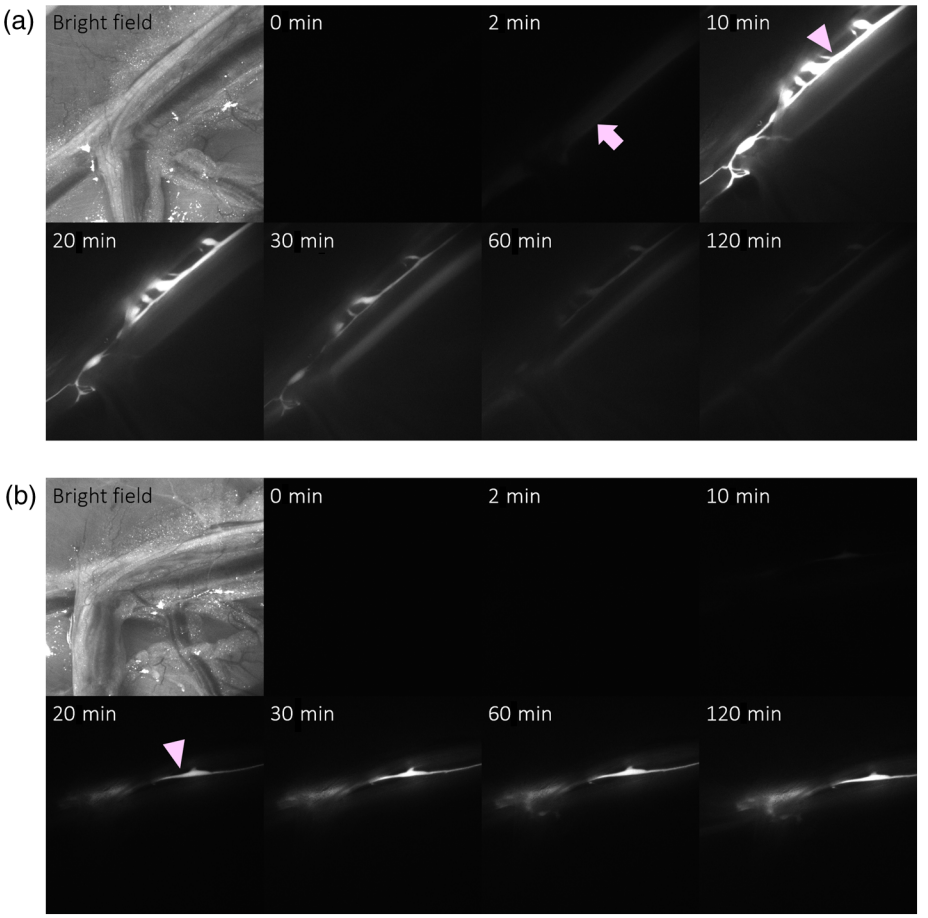

Fig. 8 Real-time fluorescence imaging; bright field images versus fluorescence images at 0 to 120 min postinjection. TK-1 and ICG were injected into the hind footpads of rats at 0 min. (a) In the TK-1-injected group, the femoral vein was visualized first (arrow, 2-min image) and successively accompanying lymphatics were detected next (arrow head, 10-min image). (b) In contrast, in the ICG-injected group, most ICG was transported via the lymphatics (arrowhead, 20-min image), and ICG in the femoral vein was not detected.

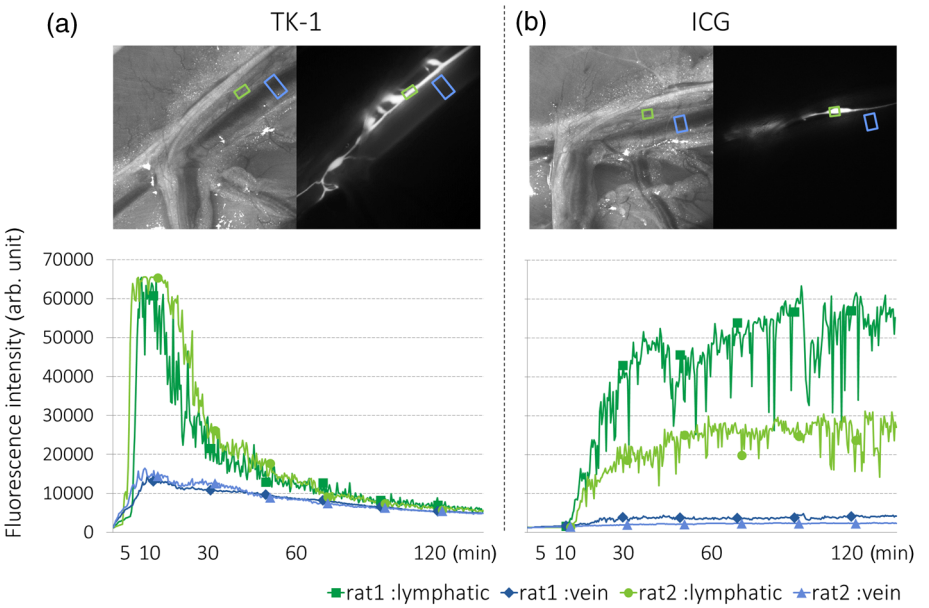

Fig. 9 Time-dependent changes of fluorescence intensities detected in the lymphatic and venous flow, with two representative cases shown for each group. The upper-left image in each group shows a bright field image, and the upper-right image shows the fluorescence. The small rectangles for the ROIs were defined, based on one of the accompanying lymphatics (green rectangles) and femoral veins (blue rectangles). The lower images show the measured fluorescence intensities of lymphatics (green lines) and femoral veins (blue lines). TK-1 and ICG were injected into the hind footpads of rats at 0 min. The transport of TK-1 via a lymphatic showed a steep peak at 10 to 15 min postinjection, which then decreased immediately to nearly the same level as observed with the femoral vein. In contrast, ICG was only transported through the lymphatics at a nearly constant rate.

undesired tissues, therefore, may interfere with surgical operations or medical diagnoses because ICG cannot be easily removed from the biological tissues to which ICG can adhere. Second, ICG can self-aggregate in water. The optical properties

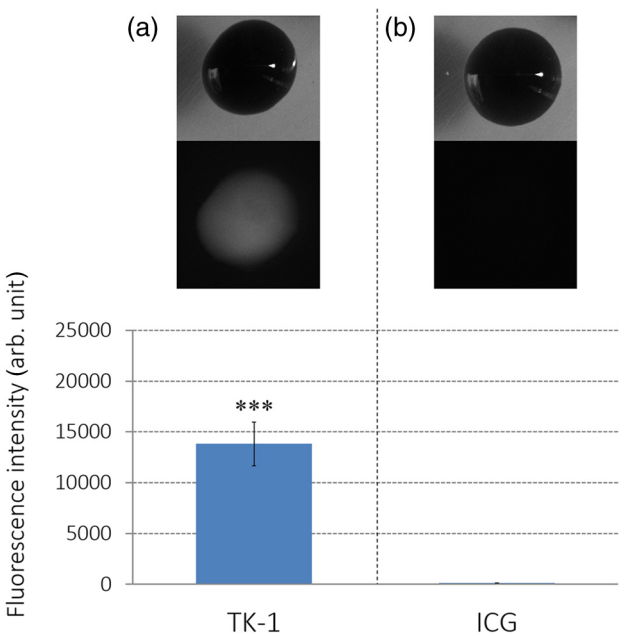

Fig. 10 Fluorescence intensity of venous blood collected at 10 min from rats in the TK-1-injected group (a) and the ICG-injected group (b). The mean fluorescence intensity in the TK-1 group was significantly higher than that measured in the ICG-injected group (***$p < 0.001$).

of ICG strongly depend on dye concentration. In aqueous solution, ICG starts to form dimers and oligomers, even at relatively low concentrations.[3,50–52] The presence of aggregates causes self-quenching of the dye, which reduces its fluorescence. In addition, ICG undergoes degradation in aqueous media resulting in the simultaneous loss of absorption and fluorescence.[5] Finally, ICG administered into living tissues immediately binds to plasma proteins, such as albumin, high-density lipoprotein, and low-density lipoprotein.[14–16] The particle size of plasma protein-bound ICG becomes ~7 to 22 nm in diameter,[16] and the vascular or tissue permeability of ICG is defined by those proteins.[16,53] Most ICG fluorescence observed in living tissues, therefore, demonstrates the *in vivo* dynamics of plasma lipoproteins, especially that of HDL alone, or in combination with LDL.[16] Thus, it is possible to study material movement only partially when using ICG.

In contrast, inorganic QDs, which are composed of a semiconductor core commonly made from CdSe or CdTe coated with an inorganic shell, have several desirable characteristics, such as nano-size particles, high quantum yields, and high chemical and optical stabilities.[22–25] Moreover, QDs are tunable, based on their size and structure, so that a narrow-width emission light can be generated across the visible and NIR spectrum, depending on the size and doping characteristics of the nanocrystals.[25] Nonetheless, issues remain that need to be addressed before these nanocrystal probes can be broadly used in biomedical applications. Importantly, the long-term biocompatibility and the potential toxicity of QDs need to be improved.[29,30,54]

The di-β-cyclodextrin-bound indocyanine derivative, TK-1, can overcome these problems. TK-1 was originally designed to mimic the absorption and fluorescence of ICG. A noteworthy feature of TK-1 is that it possesses two water-soluble

cyclodextrin molecules. Cyclodextrins are cyclic oligosaccharides produced by the enzymatic digestion of starch and are named α-, β-, and γ-cyclodextrin depending on the number of glucose units included (6, 7, or 8 glucose units, respectively). Cyclodextrins have a toroidal shape with a hydrophobic surface inside and form inclusion compounds with smaller hydrophobic compounds of appropriate size, which fit into their 0.5 to 0.8 nm cavity. These inclusion complexes have many advantages, such as increased solubility, enhanced bioavailability, and improved stability.[55–57] In this study, we expected that TK-1 would have high chemical stability, low self-aggregation, low self-quenching, and low binding to tissues because of its two β-cyclodextrin molecules. To take advantage of the cyclodextrin properties, two short carbon-chain linkers were placed between the indocyanine fluorophore and cyclodextrin. The results of our *in vitro* optical studies indicated that both hydrophilic cyclodextrin moieties of TK-1, which potentially enclose the hydrophobic indocyanine moiety, enabled TK-1 to exist as a monomer in aqueous solution (with no or low self-aggregation) and consequently to achieve high water solubility and high optical and chemical stabilities. In particular, the results from our photostability study indicated that the cyclodextrin moiety can protect the indocyanine fluorophore from photodegradation and suggested that TK-1 would be effective during lengthy *in vivo* optical imaging because of its low photobleaching property. Furthermore, we expect that TK-1 will show low nonspecific binding *in vivo*, owing to its hydrophilic cyclodextrin moieties and reduced tendency for self-aggregation. The Stoke's shift of TK-1 is much smaller than that of ICG. However, in general, when the Stoke's shift is small, the excitation and emission wavelengths will be set at slightly shorter and slightly longer wavelengths, respectively. In NIR fluorescence imaging using TK-1, a filter set optimized for ICG (ICG-B-000) can efficiently detect TK-1 fluorescence (Fig. 5). Regarding the toxicity of TK-1, we suggest that TK-1 would be as safe as ICG because it has no toxic elements in its core, in contrast to inorganic QDs. In fact, our preliminary data indicated that tail vein injection with 0.75 mg/kg TK-1 had no adverse effects in rats. Furthermore, another water-soluble indocyanine compound, which we prepared by a method similar to that used to synthesize TK-1, was nontoxic in animal experiments based on good laboratory practice (unpublished data).

As a further interesting result, our real-time *in vivo* fluorescence imaging data demonstrated that the *in vivo* dynamics of TK-1 differed markedly from those of ICG with respect to both lymphatic and venous transport. More specifically, TK-1 drained from hind footpad via the peripheral venous flow and the lymph flow, whereas ICG drained only through the lymphatics. Recently, some physiologists have concluded that the original Starling equation does not describe fluid transport adequately and that fluid reabsorption does not occur across blood vessels due to their steady-state properties; consequently, the lymphatic vasculature provides the only escape route for extravasated fluid and macromolecules.[1,58] In contrast, from a radiological point of view, it has been demonstrated that the behavior of nanoparticles injected subcutaneously is strongly dependent on their particle size.[17,18] Some studies regarding contrast agents used for magnetic resonance (MR) lymphangiography or lymphoscintigraphy have provided evidence that the particle size is the major determinant of lymphatic uptake from the interstitial fluid, and particles with small diameters (i.e., less than a few nanometers) are mostly exchanged through the blood capillaries.[19–21] In addition, regarding QDs, some authors have emphasized that the *in vivo* behavior of QDs was greatly dependent on their hydrodynamic diameters when considering renal clearance or retention in the SLN.[59–63] As noted above, the regulatory mechanism and route of solute movement are controversial. The particle size of TK-1 in aqueous solution is <3 nm. We suggest that TK-1 is probably absorbed into microvessels and lymphatics at the injection site because its particle size is smaller than that of plasma protein-bound ICG, ~7 to 22 nm. Furthermore, regarding the lymphatic transport, we found that time-dependent changes of TK-1, which showed a steep peak, were quite distinct from those of ICG. These results indicated that solute movement via the lymphatic and venous pathways can be differentially regulated, depending on the particle size. The advantage of NIR fluorescence imaging using TK-1 against MR lymphangiography or lymphoscintigraphy is that TK-1 provides real-time imaging in an inexpensive and convenient manner. In addition, the intravascular administration of TK-1 may also be valuable for NIR fluorescence imaging. In fact, we performed tail vein injection of TK-1 in rats and subsequently measured its fluorescence. The results demonstrated that TK-1 showed higher vascular permeability than ICG and could more sensitively detect mild states of localized inflammation or edema (unpublished data). We propose that TK-1 can be used to visualize the route of microcirculation, which cannot be shown by conventional ICG, and can enable real-time NIR fluorescence imaging of whole-fluid and solute movements via both the lymphatics and microvessels.

This study has some limitations. Regarding the characteristics of TK-1, we did not investigate some of its optical properties, such as the circulation time or the fluorescence lifetime. Furthermore, the following limitations should also be considered when interpreting our results. We analyzed the pharmacokinetics of TK-1 by observing the fluorescence intensities at the groin site, which is separated from the injected hind footpad; thus, we did not identify the exact peripheral route at the injected site through which TK-1 was absorbed. In addition, there is a possibility that factors other than the particle size, such as the surface charge or shape of a particle, affect the regulation of solute movement. Additional experimental methods should be devised that can solve these problems. Nevertheless, TK-1 is surely an NIR fluorescence dye, which can overcome the disadvantages of ICG, and we believe that the use of TK-1 can provide new opportunities for the visualization of microcirculation.

Acknowledgments

This project was supported by Nagoya University Hospital Funding for Clinical Research (Grant No. 716868).

References

1. V. H. Huxley and J. Scallan, "Lymphatic fluid: exchange mechanisms and regulation," *J. Physiol.* **589**(Pt 12), 2935–2943 (2011).
2. J. V. Frangioni, "In vivo near-infrared fluorescence imaging," *Curr. Opin. Chem. Biol.* **7**(5), 626–634 (2003).
3. M. L. Landsman et al., "Light-absorbing properties, stability, and spectral stabilization of indocyanine green," *J. Appl. Physiol.* **40**(4), 575 –583 (1976).
4. G. Ku and L. V. Wang, "Deeply penetrating photoacoustic tomography in biological tissues enhanced with an optical contrast agent," *Opt. Lett.* **30**(5), 507–509 (2005).

5. A. K. Kirchherr, A. Briel, and K. Mäder, "Stabilization of indocyanine green by encapsulation within micellar systems," *Mol. Pharm.* **6**(2), 480–491 (2009).
6. B. Ballou, L. A. Ernst, and A. S. Waggoner, "Fluorescence imaging of tumors in vivo," *Curr. Med. Chem.* **12**(7), 795–805 (2005).
7. C. Zhang et al., "Sentinel lymph node mapping by a near-infrared fluorescent heptamethine dye," *Biomaterials* **31**(7), 1911–1917 (2010).
8. A. Raabe et al., "Near-infrared indocyanine green video angiography: a new method for intraoperative assessment of vascular flow," *Neurosurgery* **52**(1), 132–139 (2003).
9. L. A. Yannuzzi et al., "Indocyanine green angiography-guided photodynamic therapy for treatment of chronic central serous chorioretinopathy: a pilot study. 2003," *Retina* **32**, 288–298 (2012).
10. T. Kitai et al., "Fluorescence navigation with indocyanine green for detecting sentinel lymph nodes in breast cancer," *Breast Cancer* **12**(3), 211–215 (2005).
11. F. Ogata et al., "Novel lymphography using indocyanine green dye for near-infrared fluorescence labeling," *Ann. Plast. Surg.* **58**(6), 652–655 (2007).
12. Q. Zhou et al., "Near-infrared lymphatic imaging demonstrates the dynamics of lymph flow and lymphangiogenesis during the acute versus chronic phases of arthritis in mice," *Arthritis Rheum.* **62**(7), 1881–1889 (2010).
13. N. Unno et al., "Preliminary experience with a novel fluorescence lymphography using indocyanine green in patients with secondary lymphedema," *J. Vasc. Surg.* **45**(5), 1016–1021 (2007).
14. G. R. Cherrick et al., "Indocyanine green: observations on its physical properties, plasma decay, and hepatic extraction," *J. Clin. Invest.* **39**, 592–600 (1960).
15. K. J. Baker, "Binding of sulfobromophthalein (BSP) sodium and indocyanine green (ICG) by plasma alpha-1 lipoproteins," *Proc. Soc. Exp. Biol. Med.* **122**(4), 957–963 (1966).
16. S. Yoneya et al., "Binding properties of indocyanine green in human blood," *Invest Ophthalmol. Vis. Sci.* **39**(7), 1286–1290 (1998).
17. R. T. Lucarelli et al., "New approaches to lymphatic imaging," *Lymphatic Res. Biol.* **7**(4), 205–214 (2009).
18. S. Cai et al., "Lymphatic drug delivery using engineered liposomes and solid lipid nanoparticles," *Adv. Drug Delivery Rev.* **63**(10–11), 901–908 (2011).
19. H. Kobayashi et al., "Lymphatic drainage imaging of breast cancer in mice by micro-magnetic resonance lymphangiography using a nano-size paramagnetic contrast agent," *J. Natl. Cancer Inst.* **96**(9), 703–708 (2004).
20. L. Bergqvist, S. E. Strand, and B. R. Persson, "Particle sizing and biokinetics of interstitial lymphoscintigraphic agents," *Semin. Nucl. Med.* **13**(1), 9–19 (1983).
21. S. Modi, "Human lymphatic pumping measured in healthy and lymphoedematous arms by lymphatic congestion lymphoscintigraphy," *J. Physiol.* **583**(1), 271–285 (2007).
22. S. Kim et al., "Near-infrared fluorescent type II quantum dots for sentinel lymph node mapping," *Nat. Biotechnol.* **22**(1), 93–97 (2004).
23. B. Ballou et al., "Sentinel lymph node imaging using quantum dots in mouse tumor models," *Bioconjug. Chem.* **18**(2), 389–396 (2007).
24. N. Kosaka et al., "Real-time optical imaging using quantum dot and related nanocrystals," *Nanomedicine* **5**(5), 765–776 (2010).
25. N. Kosaka et al., "In vivo real-time lymphatic draining using quantum-dot optical imaging in mice," *Contrast Media Mol. Imaging* **8**(1), 96–100 (2013).
26. X. Gao et al., "In vivo cancer targeting and imaging with semiconductor quantum dots," *Nat. Biotechnol.* **22**(8), 969–976 (2004).
27. A. C. Samia, X. Chen, and C. Burda, "Semiconductor quantum dots for photodynamic therapy," *J. Am. Chem. Soc.* **125**(51), 15736–15737 (2003).
28. R. Bakalova et al., "Quantum dots as photosensitizers?," *Nat. Biotechnol.* **22**(11), 1360–1361 (2004).
29. R. Hardman, "A toxicologic review of quantum dots: toxicity depends on physicochemical and environmental factors," *Environ. Health Perspect.* **114**(2), 165–172 (2006).
30. C. Shi et al., "Quantum dots: emerging applications in urologic oncology," *Urol. Oncol.* **26**(1), 86–92 (2008).
31. Y. Ye et al., "Multivalent carbocyanine molecular probes: synthesis and applications," *Bioconjug. Chem.* **16**(1), 51–61 (2005).
32. K. Teranishi and S. Tanabe, "Regiospecific alkylation dependent on alkyl chain length of N-bromoalkylphthalimides and an efficient preparation of 2-O-aminoalkyl cyclomaltooligosaccharides (cyclodextrins)," *ITE Lett.* **1**, 53–60 (2000).
33. C. Li et al., "Synthesis and characterization of glucosamine-bound near-infrared probes for optical imaging," *Org. Lett.* **8**(17), 3623–3626 (2006).
34. G. A. Crosby and J. N. Demas, "Measurement of photoluminescence quantum yields," *J. Phys. Chem.* **75**(8), 991–1024 (1971).
35. T. Nakamura and K. Kunita, Jpn. Kokai Tokkyo Koho, JP 2000267265 (2000).
36. Z. Zhang and S. Achilefu, "Synthesis and evaluation of polyhydroxylated near-infrared carbocyanine molecular probes," *Org. Lett.* **6**(12), 2067–2070 (2004).
37. J. G. Hauptman et al., "Measurement of hepatocellular function, cardiac output, effective blood volume, and oxygen saturation in rats," *Am. J. Physiol.* **257**(2), R439–444 (1989).
38. O. Reuthebuch et al., "Novadaq SPY: intraoperative quality assessment in off-pump coronary artery bypass grafting," *Chest* **125**(2), 418–424 (2004).
39. L. Balacumaraswami and D. P. Taggart, "Intraoperative imaging techniques to assess coronary artery bypass graft patency," *Ann. Thorac. Surg.* **83**(6), 2251–2257 (2007).
40. R. Inoue et al., "Association between the efficacy of photodynamic therapy and indocyanine green angiography findings for central serous chorioretinopathy," *Am. J. Ophthalmol.* **149**(3), 441–446.e2 (2010).
41. N. Tagaya et al. "Intraoperative identification of sentinel lymph nodes by near-infrared fluorescence imaging in patients with breast cancer," *Am. J. Surg.* **195**(6), 850–853 (2008).
42. Y. Tajima et al., "Sentinel node mapping guided by indocyanine green fluorescence imaging in gastric cancer," *Ann. Surg.* **249**(1), 58–62 (2009).
43. C. Hirche et al., "ICG fluorescence-guided sentinel node biopsy for axillary nodal staging in breast cancer," *Breast Cancer Res. Treat.* **121**(2), 373–378 (2010).
44. F. Ogata et al., "Intraoperative lymphography using indocyanine green dye for near-infrared fluorescence labeling in lymphedema," *Ann. Plast. Surg.* **59**(2), 180–184 (2007).
45. J. C. Rasmussen et al., "Lymphatic imaging in humans with near-infrared fluorescence," *Curr. Opin. Biotechnol.* **20**(1), 74–82 (2009).
46. N. Unno et al., "Quantitative lymph imaging for assessment of lymph function using indocyanine green fluorescence lymphography," *Eur. J. Vasc. Endovasc. Surg.* **36**(2), 230–236 (2008).
47. N. Unno et al., "A novel method of measuring human lymphatic pumping using indocyanine green fluorescence lymphography," *J. Vasc. Surg.* **52**(4), 946–952 (2010).
48. T. Desmettre, J. M. Devoisselle, and S. Mordon, "Fluorescence properties and metabolic features of indocyanine green (ICG) as related to angiography," *Surv. Ophthalmol.* **45**(1), 15–27 (2000).
49. R. Manchanda et al., "Preparation and characterization of a polymeric (PLGA) nanoparticulate drug delivery system with simultaneous incorporation of chemotherapeutic and thermo-optical agents," *Colloids Surf. B Biointerfaces* **75**(1), 260–267 (2010).
50. J. Zweck and A. Penzkofer, "Microstructure of indocyanine green J-aggregates in aqueous solution," *Chem. Phys.* **269**(1), 399–409 (2001).
51. F. Rotermund, R. Weigand, and A. Penzkofer, "J-aggregation and disaggregation of indocyanine green in water," *Chemistry* **96**(1), 137–148 (1996).
52. R. Philip et al., "Absorption and fluorescence spectroscopic investigation of indocyanine green," *J. Photochem. Photobiol. A Chem.* **96**(1), 137–148 (1996).
53. T. Fischer et al., "Assessment of unspecific near-infrared dyes in laser-induced fluorescence imaging of experimental arthritis," *Acad. Radiol.* **13**(1), 4–13 (2006).
54. N. Y. Morgan et al., "Real time in vivo non-invasive optical imaging using near-infrared fluorescent quantum dots," *Acad. Radiol.* **12**(3), 313–323 (2005).
55. S. Wolfram, "Cyclodextrin inclusion compounds in research and industry," *Angew. Chem. Int. Ed. Engl.* **19**(5), 344–362 (1980).
56. J. Szejtli, "Introduction and general overview of cyclodextrin chemistry," *Chem. Rev.* **98**(5), 1743–1754 (1998).

57. R. Iacovino et al., "Physicochemical characterization and cytotoxic activity evaluation of hydroxymethylferrocene: β-cyclodextrin inclusion complex," *Molecules.* **17**(5), 6056–6070 (2012).
58. C. C. Michel and M. E. Phillips, "Steady-state fluid filtration at different capillary pressures in perfused frog mesenteric capillaries," *J. Physiol.* **388**, 421–435 (1987).
59. H. S. Choi et al., "Renal clearance of quantum dots," *Nat. Biotechnol.* **25**(10), 1165–1170 (2007).
60. Y. Hama et al., "Simultaneous two-color spectral fluorescence lymphangiography with near infrared quantum dots to map two lymphatic flows from the breast and the upper extremity," *Breast Cancer Res. Treat.* **103**(1), 23–28 (2007).
61. A. Robe et al., "Quantum dots in axillary lymph node mapping: biodistribution study in healthy mice," *BMC Cancer* **8**(1), 111 (2008).
62. Y. Su et al., "In vivo distribution, pharmacokinetics, and toxicity of aqueous synthesized cadmium-containing quantum dots," *Biomaterials* **32**(25), 5855–5862 (2011).
63. A. M. Smith et al., "Bioconjugated quantum dots for in vivo molecular and cellular imaging," *Adv. Drug Delivery Rev.* **60**(11), 1226–1240 (2008).

Toshikazu Kurahashi is a chief physician assistant of the Hand and Microsurgery Center at Anjo Kosei Hospital, Japan. Between 2011 and 2015, he served at the Department of Hand Surgery, Nagoya University Graduate School of Medicine, Japan. His research interests are in hand surgery, lymphatic function and lymphedema, and near-infrared fluorescence imaging.

Katsuyuki Iwatsuki received his PhD in 2013 from the Nagoya University Graduate School of Medicine, Japan. He is an assistant professor in the Department of Hand Surgery at Nagoya University. He is a hand surgery specialist, and his research interests include lymph, neuroscience, and pain.

Tetsuro Onishi received his PhD in 2015, based on lymphedema research, from the Nagoya University Graduate School of Medicine, Japan. He is an assistant professor in the Department of Emergency Medicine and Hand Surgery at Nagoya University.

Tetsuya Arai received his PhD in 2013 from the Nagoya University Graduate School of Medicine, Japan. He is a hand surgery specialist. He specializes in microsurgery and animal operations.

Katsunori Teranishi is a professor in the Department of Life Sciences at Mie University. He has developed many novel near-infrared indocyanine dyes, one of which is TK-1.

Hitoshi Hirata is a professor in the Department of Hand Surgery, Nagoya University, Japan. He is the chief manager of many projects, one of which is focused on developing novel treatment for lymphedema.